10-2020

Detection of Reconnection Signatures in Solar Flares

Taylor R. Whitney Aegerter
National Center for Atmospheric Research

Daniel J. Emmons II
Air Force Institute of Technology
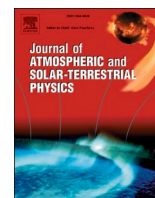
Robert D. Loper
Air Force Institute of Technology

Research Paper

Detection of reconnection signatures in solar flares

Taylor R. Whitney Aegerter [a,b,*], Daniel J. Emmons [a], Robert D. Loper [a,b]

[a] Department of Engineering Physics, Air Force Institute of Technology, 2950 Hobson Way, WPAFB, OH, 45431, USA
[b] National Center for Atmospheric Research, High Altitude Observatory, 3090 Center Green Drive, Boulder, CO, 80301, USA

ABSTRACT

Solar flare forecasting is limited by the current understanding of mechanisms that govern magnetic reconnection, the main physical phenomenon associated with these events. As a result, forecasting relies mainly on climatological correlations to historical events rather than the underlying physics principles. Solar physics models place the neutral point of the reconnection event in the solar corona. Correspondingly, studies of photospheric magnetic fields indicate changes during solar flares—particularly in relation to the field helicity—on the solar surface as a result of the associated magnetic reconnection. This study utilizes data from the Solar Dynamics Observatory (SDO) Helioseismic and Magnetic Imager (HMI) and SpaceWeather HMI Active Region Patches (SHARPs) to analyze full vector-field component data of the photospheric magnetic field during solar flares within a large HMI dataset (May 2010 through September 2019). This analysis is then used to identify and compare trends in the different categories of flare strengths and determine indications of the physical phenomena taking place.

1. Introduction

Solar flares cause disruptions to the electric and magnetic fields incident on the Earth from the Sun. In particular, this poses a danger to personnel and equipment, including Department of Defense (DoD) operations, in the space environment. Solar flares can cause disturbances within the Earth's atmosphere that can impact both natural and anthropogenic resources. Energetic particles from flares heat the atmosphere, causing it to expand and increase drag on satellites, which then forces them to expend more fuel in their orbit. Atmospheric changes as well as intensified emissions from flares can further result in degradation of satellite operations (Goddard Space Flight Center, 2020). In the ionosphere, solar flares cause Sudden Ionospheric Disturbances (SIDs), which lead to changes in electronic composition and to anomalies in signals from navigation systems and satellite communications (Liu et al., 2004; Qian et al., 2012). A study by Eastwood et al. (2017) estimates that a storm of similar level to the Carrington Event of 1859 could have an economic cost on the order of trillions of dollars in the United States alone.

Protection from these effects comes in the form of improved forecasting abilities to allow for a better reactive capability before the flare reaches the Earth or its spacecraft. Current forecasting techniques rely on climatological indications of the likelihood that a solar active region (AR) will produce a flare of a given strength. Improvements in flare forecasting can be made with greater understanding of the phenomena on the Sun that drive flare events, particularly magnetic reconnection.

The actual reconnection event occurs in the upper solar atmosphere. However, the use of photospheric data can still help improve understanding higher in the solar atmosphere. Slow photospheric—and subphotospheric—motions drive the energy supply to an AR, both through the twisting and shearing of coronal magnetic structures and through the emergence of new current-carrying magnetic flux in the photosphere (Wheatland, 2008). Furthermore, photospheric observations have previously been used to create coronal magnetic field models (Scherrer et al., 2012).

Kazachenko et al. (2017) created a database of flare ribbons, which are enhancements in Hα and 1600 Å emissions and correspond to footprints of the newly reconnected flux tubes. When compared with flare peak x-ray flux, the reconnection flux (calculated as the unsigned magnetic flux spanned by the flare ribbon) has a much stronger correlation than the unsigned AR flux.

Bobra and Couvidat (2015) applied a machine-learning algorithm to M- and X-Class flares in order to forecast these events using Helioseismic and Magnetic Imager (HMI) vector magnetic field data. Calculating performance metrics regarding the forecasting algorithm, this study determined that using four parameters with the highest feature score provides roughly the same true skill statistic as the top 13 parameters combined. These four parameters are total unsigned current helicity,

total magnitude of the Lorentz force, total photospheric magnetic free energy density, and total unsigned vertical current.

As the first decade of the HMI—onboard the Solar Dynamics Observatory (SDO)—is only just concluding, studies analyzing the entirety of the dataset or a dataset of this size are relatively uncommon. This work serves to establish an analysis of this scale.

The idea for this study originated from a case study of Labor Day (2017) storms by Loper (2018). In this case study, three of the large flares that occurred between 4 and 10 September were combined into an epoch analysis. This epoch setup serves as the foundation for the epoch analyses created in this work.

A study by Mason and Hoeksema (2010) performed a similar analysis to this study but the data used were from the Michelson Doppler Imager (MDI), the predecessor to the HMI. This study found that the gradient-weighted inversion-line length has the strongest association with flaring, but cannot produce real-time flare forecasts well. They did determine, however, that a superposed epoch analysis does have the ability to identify weak systematic responses in the data.

While these studies all focus on varying sets of parameters, their findings do indicate that there are relationships between photospheric magnetic fields and solar flares. Further, many of the results focus on stronger flares and either do not include or do not find significant results for smaller events. Although the larger flares usually have greater geo-effective conditions, expanding the study to a larger database can help to better determine the underlying physics taking place during solar flares and the associated photospheric magnetic fields.

2. Methodology

2.1. HMI data

This study uses photospheric data from the HMI onboard the National Aeronautics and Space Administration (NASA)'s SDO. Instrument description and calibration as well as data handling and scientific analysis can be found in Schou et al. (2012). Science goals, project scope, and data product descriptions can be found in Scherrer et al. (2012); Bobra and Couvidat (2015); Bobra et al. (2014).

The HMI offers many improvements to the MDI, including improved spacial and temporal resolution and the ability provide full-disk vector-field data. Observing the Fe I line (6173 Å), the instrument has an optical resolution (λ/D) of 0.91 arcseconds and is able to capture all polarizations (Scherrer et al., 2012; Schou et al., 2012).

Among available data products are HMI Active Region Patches (HARPs) and SpaceWeather HMI Active Region Patches (SHARPs), which identify and track ARs as they move across the solar disk. These datasets rely on line-of-sight (LoS) magnetogram and intensity images that are produced on a 12-min cadence. SHARP files further include 17 summary parameters of the magnetic field in the HARP (Hoeksema et al., 2014; JSOC, 2019a). Descriptions of these parameters can be found in Table 1.

Data from the HMI can be obtained from the Joint Science Operations Center (JSOC) at Stanford University (JSOC, 2019b). For this study, SHARP data are acquired using the Python notebook created by Glogowski and Bobra (2016). The dataset in this study begins in May 2010, when HMI was first operational (Schou et al., 2012). SHARP data were collected through September 2019, providing nearly a decade of solar flares for analysis. This time period covers the majority of solar cycle 24.

2.2. Flare data

The Space Weather Prediction Center (SWPC) at the National Oceanic and Atmospheric Administration (NOAA) maintains an archive of solar events (SWPC, 2019). These are automatically identified by Geostationary Operational Environmental Satellite (GOES) spacecraft using a detection algorithm and supplemented by forecaster input as

Table 1

SHARP parameters, descriptions, and calculations (Adapted from Hoeksema et al., 2014; Bobra et al., 2014; JSOC, 2019a, 2019c).

Keyword	Description	Unit	Formula
AREA_ACR	De-projected area of active pixels	μH	$A_{total} = \sum dA$
USFLUX	Total unsigned flux	*Maxwells*	$\varphi = \sum \lvert B_z \rvert dA$
MEANGAM	Mean inclination angle	*Degrees*	$\overline{\gamma} = \frac{1}{N} \sum \tan^{-1}\left(\frac{B_h}{B_z}\right)$
MEANGBT	Mean value of the total field gradient	*G/Mm*	$\overline{\lvert \nabla B_{tot} \rvert} = \frac{1}{N} \sum \sqrt{\left(\frac{\partial B}{\partial x}\right)^2 + \left(\frac{\partial B}{\partial y}\right)^2}$
MEANGBZ	Mean value of the vertical field gradient	*G/Mm*	$\overline{\lvert \nabla B_z \rvert} = \frac{1}{N} \sum \sqrt{\left(\frac{\partial B_z}{\partial x}\right)^2 + \left(\frac{\partial B_z}{\partial y}\right)^2}$
MEANGBH	Mean value of the horizontal field gradient	*G/Mm*	$\overline{\lvert \nabla B_h \rvert} = \frac{1}{N} \sum \sqrt{\left(\frac{\partial B_h}{\partial x}\right)^2 + \left(\frac{\partial B_h}{\partial y}\right)^2}$
MEANJZD	Mean vertical current density	mA/m^2	$J_z \propto \frac{1}{N} \sum \left(\frac{\partial B_y}{\partial x} - \frac{\partial B_x}{\partial y}\right)$
TOTUSJZ	Total unsigned vertical current	A	$J_{z_{total}} = \sum \lvert J_z \rvert dA$
MEANALP	Characteristic twist parameter, α	$1/Mm$	$\alpha_{total} \propto \frac{\sum J_z B_z}{\sum B_z^2}$
MEANJZH	Mean current helicity	G^2/m	$\overline{H_c} \propto \frac{1}{N} \sum B_z J_z$
TOTUSJH	Total unsigned current helicity	G^2/m	$H_{c_{total}} \propto \sum \lvert B_z J_z \rvert$
ABSNJZH	Absolute value of the net current helicity	G^2/m	$H_{c_{abs}} \propto \lvert \sum B_z J_z \rvert$
SAVNCPP	Sum of the absolute value of the net currents per polarity	A	$J_{z_{sum}} \propto \left\lvert \sum^{B_z^+} J_z dA \right\rvert + \left\lvert \sum^{B_z^-} J_z dA \right\rvert$
MEANPOT	Mean photospheric excess magnetic energy density	erg/cm^3	$\overline{\rho} \propto \frac{1}{N} \sum (\vec{B}^{Obs} - \vec{B}^{Pot})^2$
TOTPOT	Total photospheric magnetic energy density	erg/cm	$\rho_{total} \propto \sum (\vec{B}^{Obs} - \vec{B}^{Pot})^2 dA$
MEANSHR	Mean shear angle	*Degrees*	$\overline{\Gamma} = \frac{1}{N} \sum \cos^{-1}\left(\frac{\vec{B}^{Obs} \cdot \vec{B}^{Pot}}{B^{Obs} B^{Pot}}\right)$
SHRGT45	Percentage of pixels with a mean shear angle greater than 45°	*Percent*	$\frac{area\ with\ shear > 45°}{HARP\ area}$

needed (SWPC, 2009). This archive is publicly available at (2019) and includes solar flare times, intensities, and NOAA AR numbers used in this study, among additional event data.

Flare start times were used preferentially over maximum times as the imagery would have been impacted at the maximum time with the flare already in progress. Furthermore, the time between beginning and maximum of a flare varies for each event. As a result, the data leading up to flare maximum cannot be accurately categorized as part of the flare itself or as part of the lead-up for a dataset of this size (Gibson et al., 2019).

The first entry in the HARP dataset is dated May 1, 2010. Data were collected through September 2019, but the last HARP recorded in this time ends on September 4, 2019. In this dataset, there were 13,508 flares recorded. Of these flares, 5493 were B-Class, 7210 were C-Class, 697 were M-Class, and 46 were X-Class. The remainder were A-Class and unused in this study. The distribution of flare strengths peaks strongly at C1.2, of which there are 519 flares, as seen in Fig. 1. As in the study by Wheatland (2008), there is a power-law distribution of flare strengths.

Due to the logarithmic scale of flare classes, the bin size increases for each successive category. Each stronger class has a larger bin size (e.g.
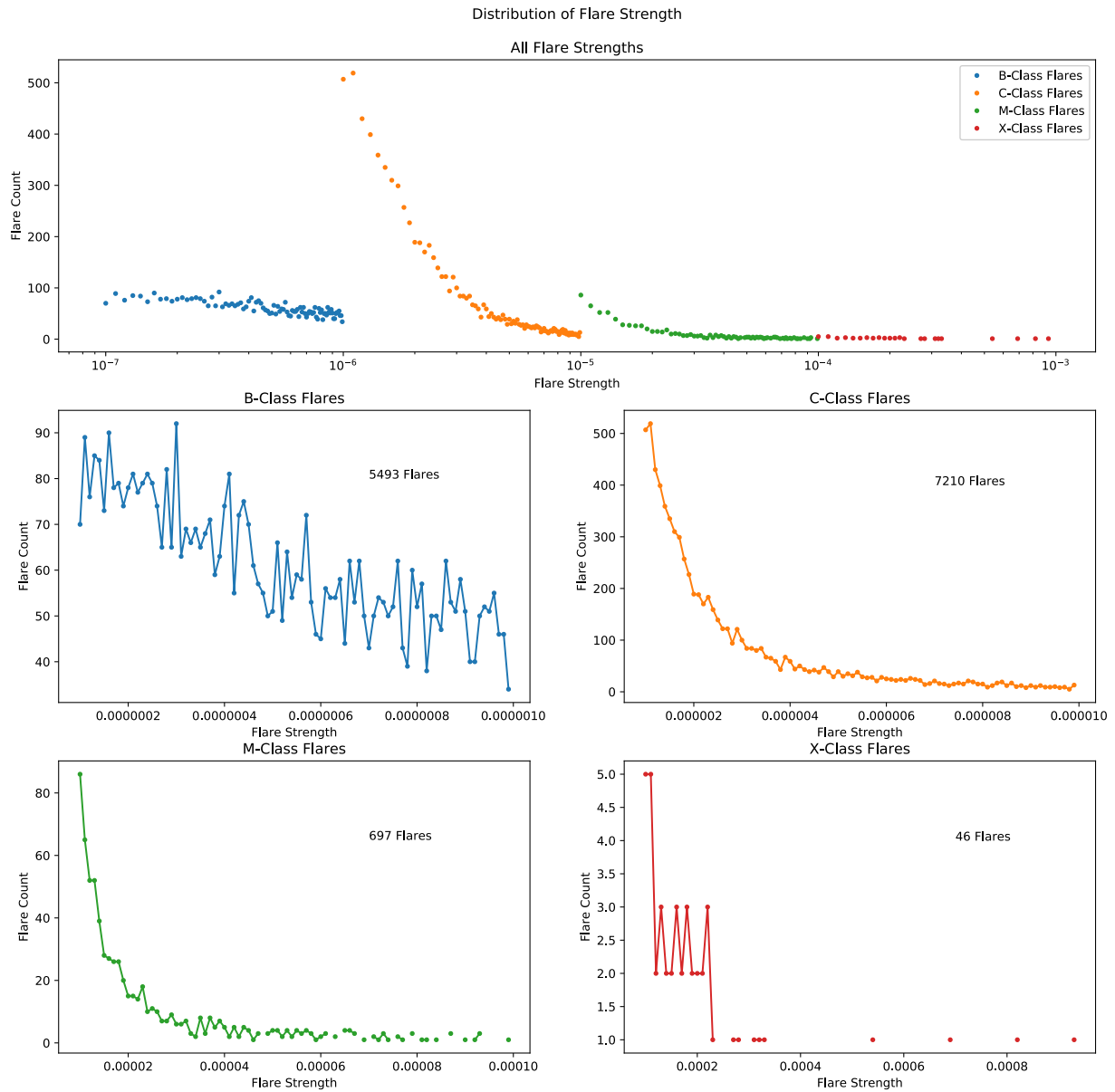
Fig. 1. Distribution of flare strength in the dataset spanning May 2010–September 2019. The top plot is a semi-logarithmic plot in the x-axis to match the scale for flare classification. The bottom four plots show individual distributions of each flare class. The strength distribution peaks at C1.2 with 519 flares. Flare strengths are identified by (2019).

the change in flux from B1 to B2 compared to the change in flux from C1 to C2) by a factor of ten and thus has a wider range of flares counted. As a result, there is a discontinuity between each class in the distribution of flare strengths, seen in Fig. 1.

The B-Class flares do not appear to follow the same distribution. B-Class flares are more easily washed out by stronger or a high frequency of flares (Gibson et al., 2019) or by the background x-ray flux during solar max. In these instances, any B-Class flares would not be identified by the SWPC detection algorithm. As a result, especially near solar maximum, the B-Class flares that are recorded do not represent the greater number that actually occur.

The SHARP and SWPC datasets were associated to extract SHARP data for 2 h prior to and 4 h following a flare. The isolated epoch flare data was then parsed to eliminate outlier events. This was done separately for all flares as well as for subsets of each flare class. With these adjustments, events were plotted for trend analysis.

2.3. Statistical analysis

2.3.1. Eliminating outliers

For plotting the epoch analyses of the dataset, two masks were applied to remove outliers. Masks were applied separately for each compilation of epoch data—for the full dataset as well as the flare class subsets. The first mask was to eliminate flares outside of three standard deviations from the average value. Flares were discarded if any parameter at any time step in the 6-h epoch window was outside of the standard deviation limits. When included, these flares dominated the dataset, falsely skewing the results. Standard deviation limits applied for each parameter, normalized to the flare time values, can be found in Fig. 2.

Next, flares outside of 70° longitude were eliminated. Longitudinal masks serve to eliminate data in which the LoS magnetic fields measured by the HMI are falsely dominated by horizontal rather than radial magnetic fields as well as data impacted by apparent solar limb effects. Limb darkening results from the variation of the depth surveyed in an
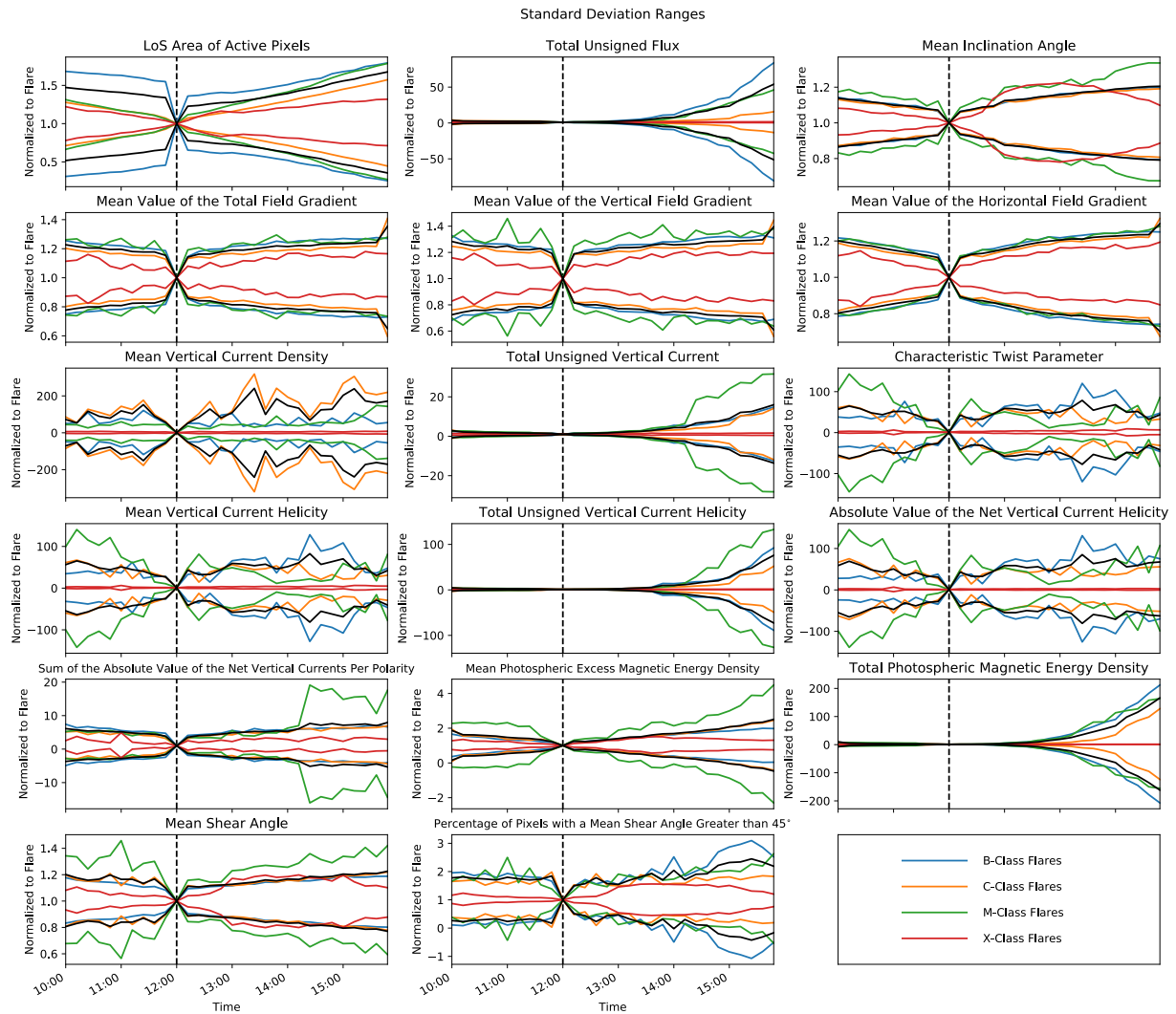
Fig. 2. Standard deviation limits applied to the dataset and subsets for this study. Data outside these limits are disregarded for this study. Plotted lines represent three standard deviations from the average values of a given subset. Each color represents a different subset: all flares in black, B-Class flares in blue, C-Class flares in orange, M-Class flares in green, and X-Class flares in red. Values are normalized to flare start times, denoted by the vertical dashed line. SHARP data are acquired from JSOC using the Python notebook created by Glogowski and Bobra (2016) and flare times are identified by (2019).

image due to the optical depth of the plasma and the geometry of the LoS, affecting all pixels at a given radius. Foreshortening affects only the sunspots, but results in a distortion of the spot near the limb as the LoS looks across the sunspot rather than directly onto it.

Studies of solar events, such as Kazachenko et al. (2017) and Bobra and Couvidat (2015), include similar limits to their data. In the study by Kazachenko et al. (2017), a limit of 45° longitude was applied. This was to exclude magnetic field data that were more transverse than radial, with respect to LoS. Meanwhile, Bobra and Couvidat (2015) apply a mask of 70° from central meridian as the signal-to-noise ratio in the SHARP parameters significantly increases beyond this longitude (Bobra et al., 2014). In a study by Criscuoli et al. (2017) regarding network and faculae from the same dataset, observations are included as far out as 78° but a deconvolution is performed to compensate for the scattered light effects near the solar limb. The remainder of the solar limb is disregarded only due to uncertainties in this region.

To determine the longitude mask best suited for this study, sets of plots were created with 45° and 70° masks as well as no mask. Comparison of these plots showed no significant differences between the masks, with fluctuations within a few percent. This indicates that the SHARP calculations do make corrections for longitude in the Stokes parameters. This correction is necessary in the HARP dataset as it tracks

ARs to the limbs in order to maintain HARP history across the Earth-facing solar hemisphere (JSOC, 2019a). The 70° mask was used for this study in order to avoid lost or incomplete patches as they rotate onto and off the solar disk as well as to avoid some of the more extreme limb effects to the data.

After eliminating outliers, the dataset is still dominated significantly by weak C-Class flares, so much so that the C1 and C2 flares comprise 40% of the events considered. Further, despite the undersampling of B-Class flares, they still make up a larger portion of the dataset than either the M- or X-Class flares. Moreover, flares with a strength of X4 and greater are outside the limits of the applied masks. Prior to the masks, there were only four flares in this range: an X5.4, an X6.9, an X8.2, and an X9.3. The X6.9 and X8.2 flares were too close to the solar limb and the other two were beyond standard deviation limits, overpowering the general X-Class flare behavior.

2.3.2. Displaying data

In order to compare the events, all parameters were normalized to the value of each flare at its start time. This allows all the events to be displayed on the same scale and shows the changes relative to the flare onset. While the flare maximum time is used to determine flare strength and is typically the time associated with the event, the start time was

used instead to avoid contamination of the data from the ongoing flare (discussed in Section 2.2).

Due to the substantial quantity of flares in the dataset, displaying them all on a single plot gives a crowded plot on which it is difficult to determine any trends. To summarize the dataset, averages and medians of the data for each point in time across all flares of a given strength were plotted. Median plots are used in this study and can be found in Section 3. Average plots were not used for this study. Medians were chosen over averages since the data follow a power law distribution in which averages are more susceptible to outliers and may not provide an adequate representation.

2.4. Limitations

This study only considers flares that have an associated NOAA AR. The association is performed during the SHARP analysis and can be accessed through the header of the data file in the same manner as the SHARP parameters used in this study. Of the 13,508 flares that occurred between May 2010 and September 2019, 2890 did not have an associated NOAA AR; this is approximately 21% of the dataset.

In the SWPC archive of solar events, there are seven occasions when the maximum time of the flare was missing, denoted as "////." For all of these events, the begin times were around or after 23:40 and the end times were around or before 00:05 the next day. In these instances, the maximum times were set to 00:00.

As previously mentioned, magnetic reconnection occurs in the upper solar atmosphere while the observations analyzed here are of the photosphere. In order to get a fuller picture of reconnection events, chromospheric and coronal observations must also be considered. Furthermore, solar flares can change the opacity of the solar atmosphere, impacting the accuracy of the photospheric observations and potentially contaminating the data for times during and immediately following a flare.

While the HMI is the first instrument to continuously measure full-disk observations of the solar magnetic field in all orientations (Stanford University, 2019)—an immeasurable value to the advancement of scientific understanding of the Sun—the SHARP catalog is limited to a 12-min cadence between observations (JSOC, 2019c, 2020). This is because the magnetograms are created using multiple sequences of registered filtergrams, combined using circularly polarized exposures (JSOC, 2020). There are multiple limitations as a result:

- Motions and changes in the magnetic field that occur on time scales less than 12 min will be lost
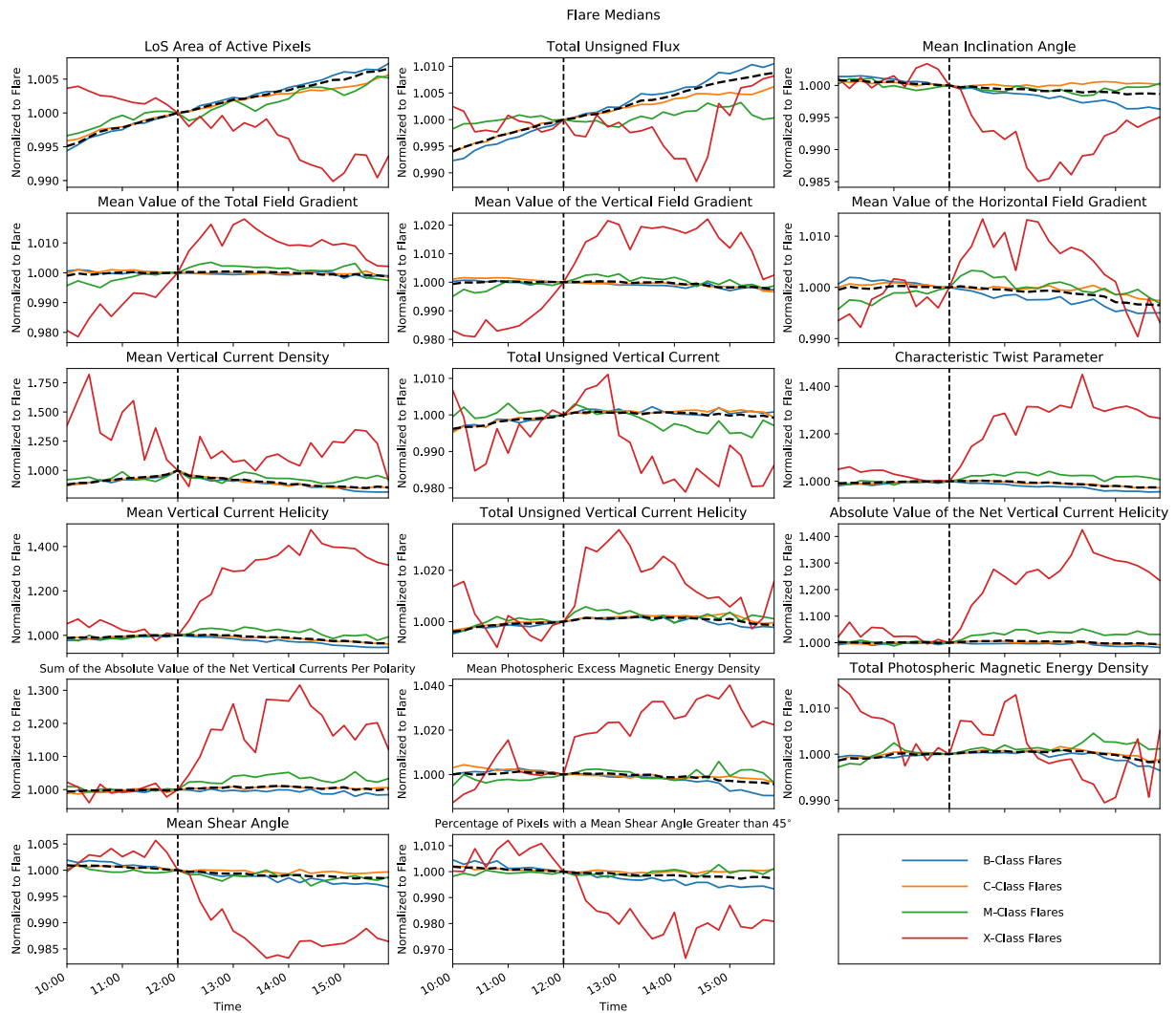
Fig. 3. Epoch analysis for all flares between May 2010 and September 2019. All data are normalized to the values at the time of the flare, which is identified as the dashed vertical line. Strengths of flares are separated by corresponding colors. The plots display medians for all events in the associated flare class. Flares outside of three standard deviations from the average and outside of 70° heliographic longitude are excluded as outliers. SHARP data are acquired from JSOC using the Python notebook created by Glogowski and Bobra (2016) and flare times are identified by (2019).

- Observations may be partly or fully affected by the occurrence of a flare during the time between measurements
- For flares that occur between measurements, the times were attributed to the nearest observation time
  - Flare times may be incorrect by as many as 6 min
  - The nearest observation time may be after the start time of the flare, thus resulting in the aforementioned contamination of the data due to the ongoing flare.

3. Analysis

Results for all flares considered in the study can be found in Fig. 3. The plots are all in the same time scale, beginning 2 h before each flare and concluding 4 h after. Arbitrarily, this time window is set as 10:00 to 16:00. The flare time, denoted on the x-axis as 12:00, is represented by the vertical dashed line. The plot of median values of all flares considered is the thick, dashed line. Each of the colored lines represents the median values of the subsets of data that are separated by flare class: blue for B-Class flares, orange for C-Class flares, green for M-Class flares, and red for X-Class flares.

Given that the variability of the X-Class flares prohibits the ability to see trends in smaller flares that are concentrated around the overall

median values, the same plots can be see in Fig. 4 without the X-Class flares. The scale of the y-axis is set to adjust based on the data displayed, so it shows a much smaller range without the large flares.

Another means of visualizing the data is given in Fig. 5. This scatter plot gives the differences from start to end of the epoch time on the y-axis and flare strength along the x-axis. Each of the colors corresponds to flare class, as in Fig. 3. Similarly, Fig. 6 shows the differences in parameters from start to end time of the flare on the y-axis. This method shows the variability across flare strengths that is lacking in Figs. 3 and 4 as all flares studied are shown. Correspondingly, Figs. 7 and 8 compare the flare duration to the parameter differences and flare strength, respectively. Parameter values are normalized to flare start time.

3.1. Results

For all parameters, the X-Class flare trends differ from the smaller flare trends. Furthermore, the M-Class flare trends for some parameters or part of the epoch timeline differ from the smaller flares. In these instances, the overall trends are similar to the X-Class flares but to a smaller extent. A similar result was found in Mason and Hoeksema (2010) in which the percent changes in calculated parameters were greater for X-Class flares while the M-Class flares and lower had similar
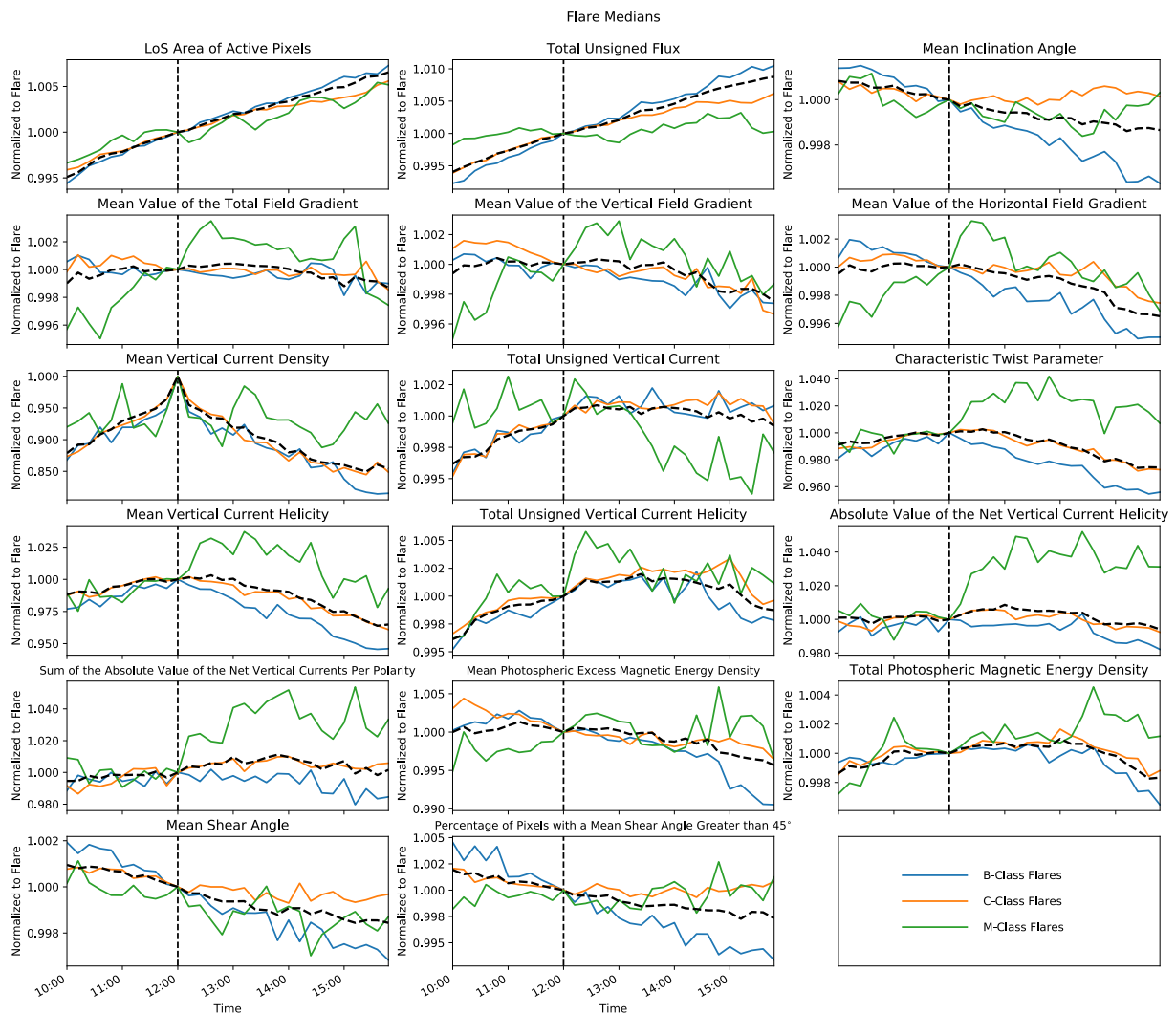
Fig. 4. Epoch analysis for all but X-Class flares between May 2010 and September 2019. All data are normalized to the values at the time of the flare, which is identified as the dashed vertical line. Strengths of flares are separated by corresponding colors. The plots display medians for all events in the associated flare class. Flares outside of three standard deviations from the average and outside of 70° heliographic longitude are excluded as outliers. SHARP data are acquired from JSOC using the Python notebook created by Glogowski and Bobra (2016) and flare times are identified by (2019).
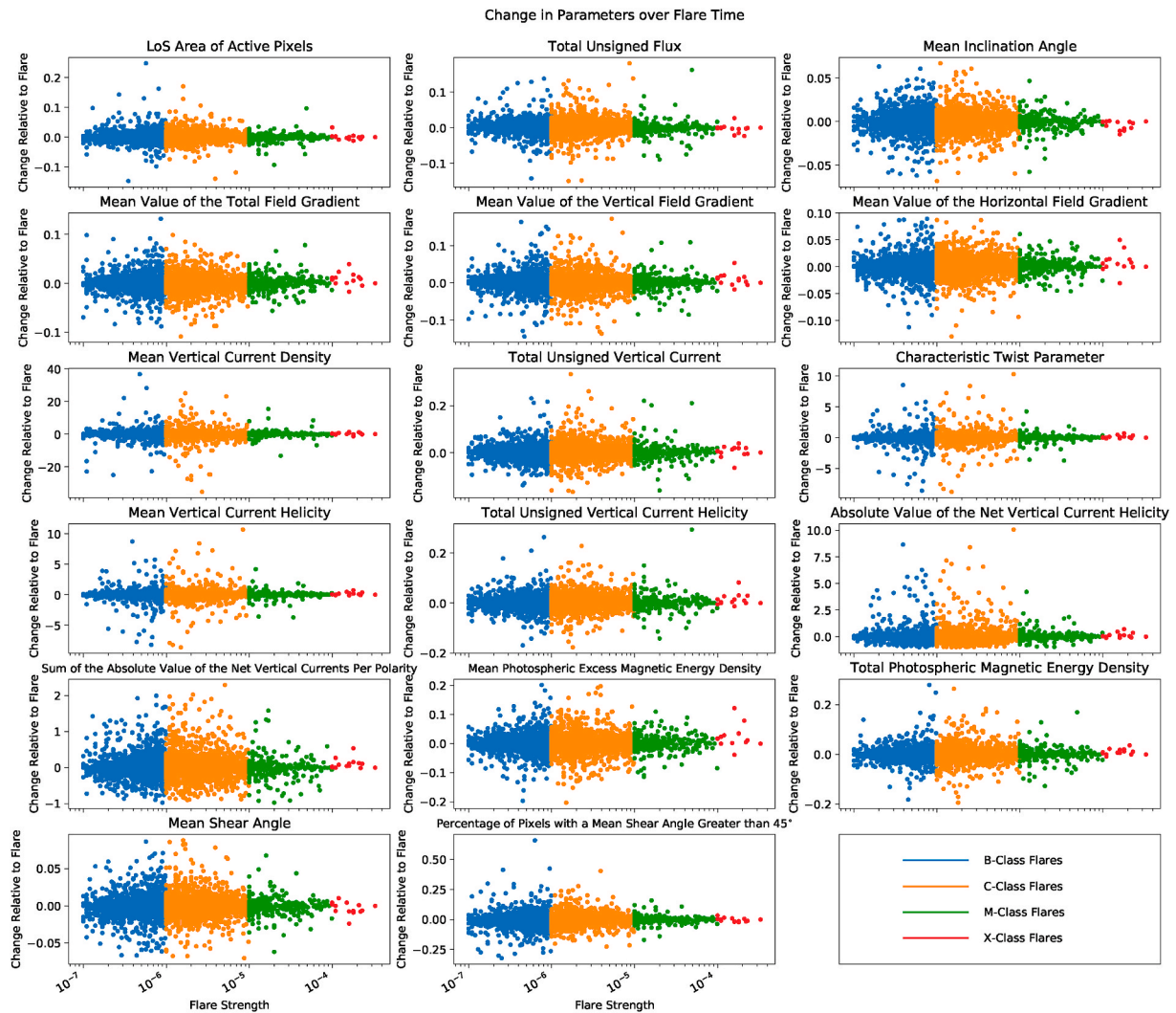
Fig. 5. Differences in normalized parameter values from 2 h prior to 4 h after the start time of a flare. Strengths of flares are along the semilogarithmic x-axis and separated by flare class with corresponding colors. Flares outside of three standard deviations from the average and outside of 70° heliographic longitude are excluded as outliers. SHARP data are acquired from JSOC using the Python notebook created by Glogowski and Bobra (2016) and flare times are identified by (2019).

changes. This indicates that the large flares are outliers among solar flares. Interestingly, the changes from the start to end of the epoch analysis and of the flare duration show greater variation among smaller flares than larger for all parameters (Figs. 5–7).

The greatest change over the duration of the flare (Figs. 6 and 7) manifests in the mean vertical current density, with multiple instances of changes up to 40 times greater or less than the value at the flare start. The majority of the events are within 20 times the start value, which still provides the greatest change in parameter value. The next closest are the characteristic twist parameter, mean vertical current helicity, and absolute value of the net vertical current helicity, whose changes are concentrated within 10 times the initial value.

Fig. 8 shows that the majority of flares last for less than 100 min. The longest flares seem to be the upper-B-Class and lower-C-Class flares, which is also where the strength distribution peaks (Fig. 1). Moreover, the shortest flares change the most over the duration of the flare (Fig. 7). Given that these shortest flares comprise a majority of the dataset, they are likely to best represent flare magnetic field properties.

3.2. Discussion

The B-, C-, and M-Class flares increase in size and unsigned flux throughout the entire epoch analysis, indicating that the ARs are

growing while the X-Class flare ARs might have reached a maximum in size and strength. Additional trends suggest that there are differences in the underlying physics associated with small and large flares. The behavior of the X-Class and, to a lesser extent, the M-Class flares differs from that of the B- and C-Class flares. Within the sub-classes of M-Class flares, there appears to be a change from behaviors of smaller flares to those of larger flares.

Most notably, the twist and helicity parameters have a significant increase after the onset of a strong flare. This indicates greater twisting of the magnetic field lines following the flare, perhaps a reaction to untwisting during the flare. There is also an intensifying throughout these flare processes, seen by the increase in the gradient parameters. These flares demonstrate extreme reactions following the event, compared to smaller flares. During the flare itself, these more intense events could be obliterating the corresponding ARs.

Consistent with Bobra and Couvidat (2015), parameters focusing on total unsigned vertical current are among those with the strongest visible trends. From this study, the helicity parameters as well as the twist parameter, in particular, exhibit similar trends. Of note, however, Bobra and Couvidat (2015) find these parameters to be beneficial for flare forecasting, while this study indicates that the trends are better seen following the flare.

For the purposes of flare forecasting, few of the parameters give an
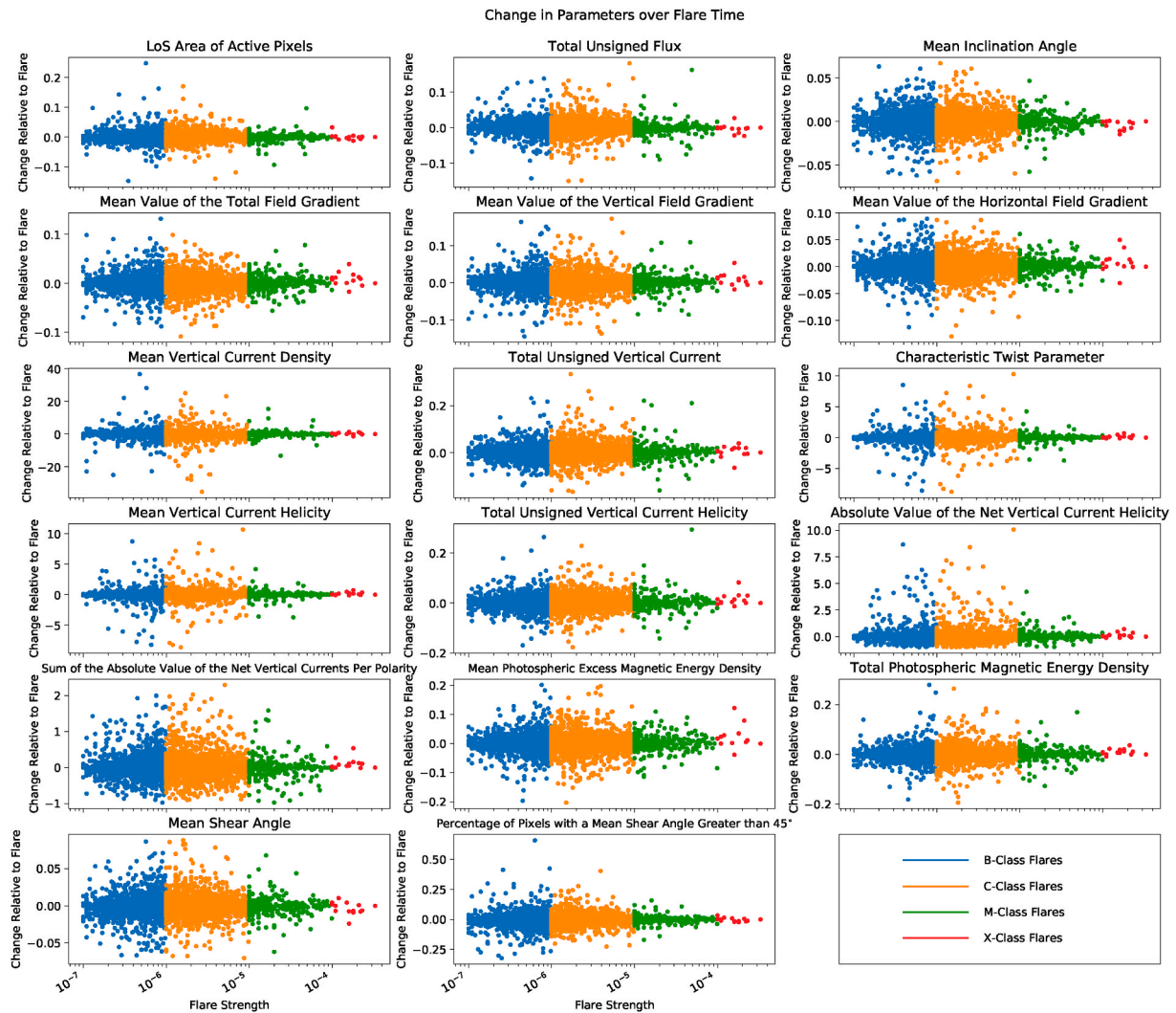
Fig. 6. Differences in normalized parameter values from the start to end time of a flare. Strengths of flares are along the semilogarithmic x-axis and separated by flare class with corresponding colors. Flares outside of three standard deviations from the average and outside of 70° heliographic longitude are excluded as outliers. SHARP data are acquired from JSOC using the Python notebook created by Glogowski and Bobra (2016) and flare times are identified by (2019).

overwhelming signature associated with an imminent flare, with the exception of the mean vertical current density. The strong increase leading into the flare start may give an early indication of an AR that is soon to flare, increasing as much as a full percent within the hour prior to the flare. For the M-Class flares, there are other spikes in the data for this parameter that may provide false-positive forecasts. However, this parameter may be of significant use for forecasting of B- and C-Class flares.

Given this flare forecasting potential, the sample size of C-Class flares (Fig. 1), and the disparity between strong and weaker flares, studies focusing on C-Class flares could help improve understanding of the physics involved. M- and X-Class flares are typically the focus of studies and forecasts, namely due to the more extreme impacts. However, because these larger flares are less frequent, they do not lend themselves to sample sizes useful in rigorous statistical analyses but rather to case studies. Additionally, the greater energy outputs from M- and X-Class flares tend to perturb the solar atmosphere more greatly, and their impacts on opacity and chemistry are not well known (Gibson et al., 2019).

Conversely, B-Class and weaker flares are typically drowned out during solar maximum by the background X-ray flux, so they are also not well suited to rigorous statistical analyses. C-Class flares appear to fall into a sort of "Goldilocks range" that provides frequent enough data for statistical analyses, perturbs the solar atmospheric properties less

severely than stronger flares, and potentially shows enough of their behavior to enable studies of fundamental flare processes. Thus, a focus on C-Class flares should be emphasized.

4. Conclusions and future work

4.1. Summary

For the purposes of understanding the underlying physics, certain trends can be identified. The rise in both size and flux levels of small and moderate flares indicates that these ARs may still be growing in size and strength while producing flares. The X-Class flares, however, seem to be doing the opposite, perhaps suggesting that they have reached a maximum size or strength. Trends in the field gradients for M- and X-Class flares demonstrate the intensifying of the magnetic structures during the flare process. Similarly, the sudden increase in helicity parameters and characteristic twist parameter following M- and X-Class flares implies an increase in the complexity of the magnetic field configuration. Extreme responses of X-Class flare ARs suggests that they get obliterated by the flares.

Coupled with the changes noted in Figs. 5 and 6, in which helicity and twist parameters show greatest variability throughout the flare duration, these parameters provide a strong signal for investigation into
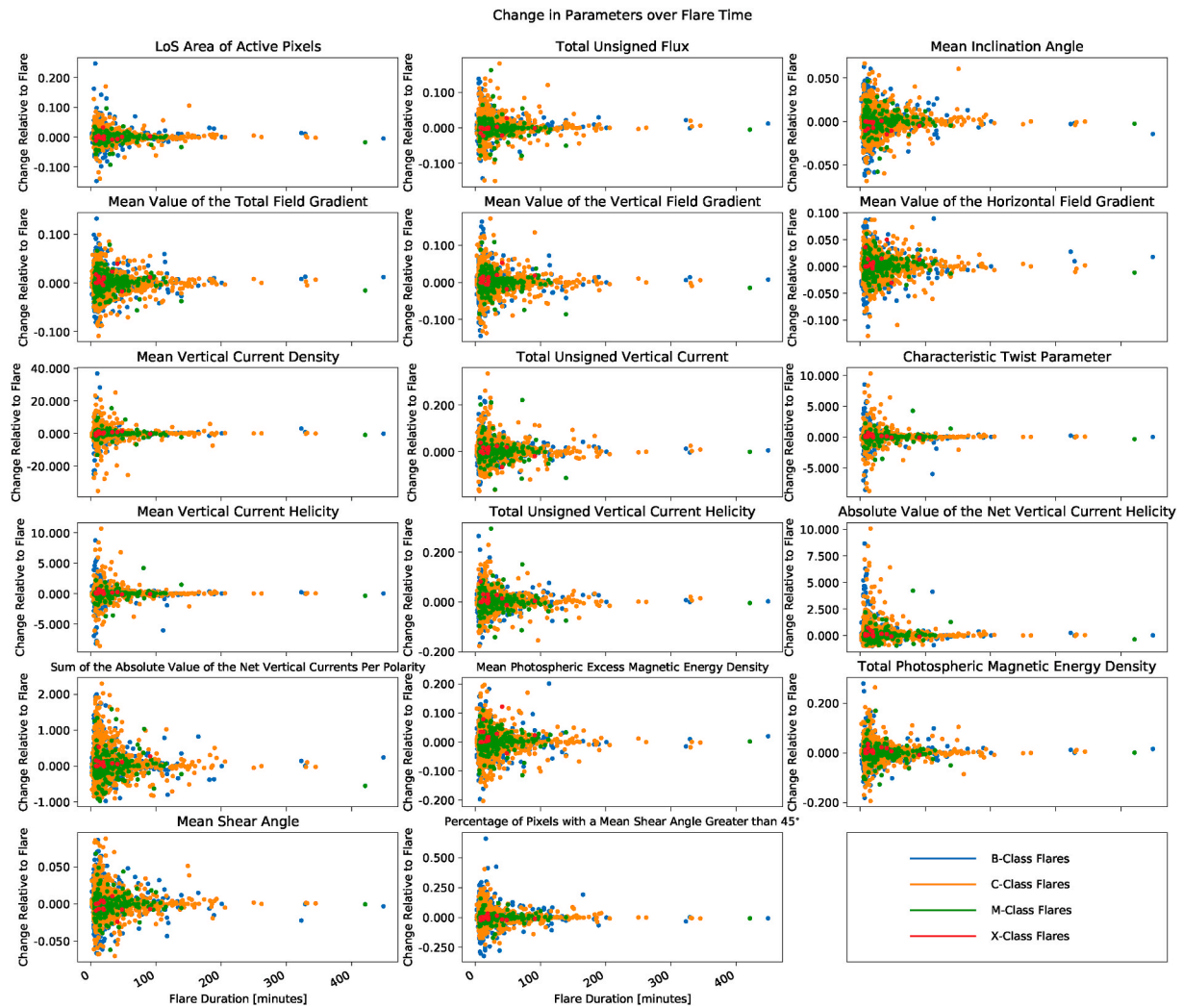
Fig. 7. Differences in normalized parameter values from start to end time of a flare compared to the duration of the flare. Durations of flares are along the x-axis in minutes and separated by flare class with corresponding colors. Flares outside of three standard deviations from the average and outside of 70° heliographic longitude are excluded as outliers. SHARP data are acquired from JSOC using the Python notebook created by Glogowski and Bobra (2016) and flare times are identified by (2019).

the physics of flares. Of note, these all rely on the vertical current density, but the mean vertical current density and total unsigned vertical current parameters do not exhibit similar patterns in the epoch analysis (Figs. 3 and 4). The mean vertical current density does show the greatest variability in the change over the course of the flare (Figs. 6 and 7).

As previously stated, Fig. 3 suggests that X-Class flares are outliers among the dataset. Furthermore, the shorter events, particularly of the B-, C-, and M-Class flares, exhibit the greatest variability and makeup the majority of the dataset (Figs. 7 and 8). Given that the B-Class flares are harder to sample and often left out of databases (Fig. 1) and that M-Class flares follow similar trends to the X-Class flares, both with small sample sizes (Fig. 4), the C-Class flares prove to be a significant subset of the overall dataset. Moving forward, studies focused specifically on C-Class flares may provide more useful indications of basic flare physics.

For the purposes of forecasting flares, however, few of these parameters show strong patterns. The most significant trend leading into a flare seems to be the mean vertical current density, particularly for B-, C-, and M-Class flares. This could be helpful as these flares are often harder to predict. Anecdotally, large flares can be expected from extremely complex ARs with only a question of timing whereas smaller and less complex ARs have a higher chance of not producing a flare. However, the signature manifests within the hour leading into the flare, which does not give much of a lead time for the flare forecast.

4.2. Future work

4.2.1. Flare classification

The current flare classification separates events based solely on their maximum x-ray flux. Apart from general trends, this classification does not adequately separate flares by common behavior. Furthermore, due to the high volume of flares in the HMI dataset, it is difficult to determine overall trends. Separating the flares based on commonalities between the events or ARs would serve to better classify flare types and trends and could benefit flare forecasting. For example, a flare classification based on AR properties could be used by forecasters to identify possible events produced from similar observations in real time. Some of the ways that the flare database could be further broken down in order to assess trends include:

- Comparing flares that occur as the AR is near solar meridian to those that occur when the AR is near solar limbs
- Correlating flares with geo-effective events such as coronal mass ejections (CMEs) and compare to flares without these events
- Determining whether the occurrence of a precursor flare, as in Verma (2018), impacts the resulting parameters
- Studying the differences in flare properties throughout the evolution of the AR lifetime.
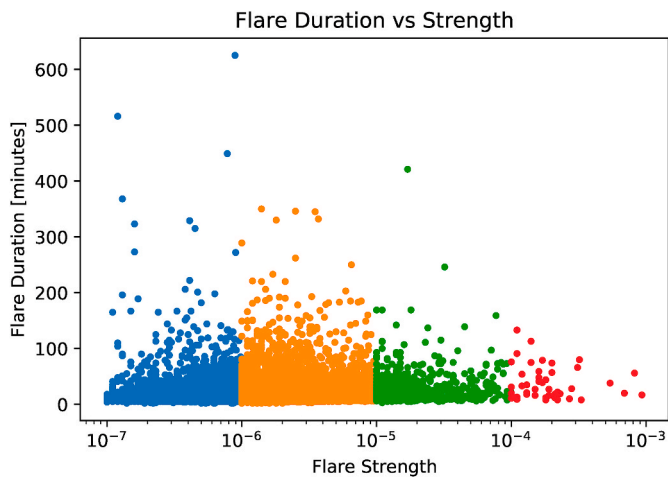
Fig. 8. Duration of flares compared to their strengths. Strengths of flares are along the semilogarithmic x-axis and separated by flare class with corresponding colors. Flares outside of three standard deviations from the average and outside of 70° heliographic longitude are excluded as outliers. SHARP data are acquired from SHARP using the Python notebook created by Glogowski and Bobra (2016) and flare times are identified by (2019).

4.2.2. Statistical analysis

The statistical analysis performed in this study is limited to basic statistics, namely means, medians, and standard deviations. However, further research into the distribution of the parameters for a given time across flare strengths—and appropriate analysis—could better provide a characterization of the parameters in question.

Another improvement to statistical analysis of these flares could be to further mask the imagery to isolate the parts of the AR that most impact the magnetic reconnection. One option would be to use the flare ribbon database created by Kazachenko et al. (2017) to then calculate magnetic parameters for the footprints of the reconnection flux tubes. A similar option would be to identify the polarity inversion line and calculate the parameters for pixels identified along that line in order to eliminate pixels in the AR that contain weak magnetic fields, as in Bobra and Couvidat (2015) and Mason and Hoeksema (2010).

In a similar matter, improving the spatial scope of the events considered would include more events. To be able to accurately use data with greater deviations from disk center, a deconvolution algorithm to compensate for limb darkening effects such as that in Criscuoli et al. (2017) could be applied. Improving flare statistics and categorizations can provide greater trend analysis for both improved physics understanding and forecasting abilities of solar flares of all strengths.

Declaration of competing interest

The authors declare that they have no known competing financial interests or personal relationships that could have appeared to influence the work reported in this paper.

Acknowledgements

References

Bobra, M.G., Couvidat, S., 2015. Solar flare prediction using SDO/HMI vector magnetic field data with a machine-learning algorithm. Astrophys. J. 798, 135.

Bobra, M.G., Sun, X., Hoeksema, J.T., Turmon, M., Liu, Y., Hayashi, K., Barnes, G., Leka, K., 2014. The helioseismic and magnetic imager (HMI) vector magnetic field pipeline: SHARPs–space-weather HMI active region patches. Sol. Phys. 289, 3549–3578.

Criscuoli, S., Norton, A., Whitney, T., 2017. Photometric properties of network and faculae derived from HMI data compensated for scattered light. Astrophys. J. 847, 93. https://doi.org/10.3847/1538-4357/aa8ad7. https://doi.org/10.3847/F1538-4357/Faa8ad7.

Eastwood, J., Biffis, E., Hapgood, M., Green, L., Bisi, M., Bentley, R., Wicks, R., McKinnell, L.A., Gibbs, M., Burnett, C., 2017. The economic impact of space weather: where do we stand? Risk Anal. 37, 206–218.

Gibson, S., Leka, K., Kazachenko, M., 2019. Personal Conversation on 30 October 2019.

Glogowski, K., Bobra, M.G., 2016. A New Python Module for Accessing HMI and AIA Data. http://hmi.stanford.edu/hminuggets/?p=1757. (Accessed 9 October 2019).

Goddard Space Flight Center, 2020. The Impact of Flares. https://hesperia.gsfc.nasa.gov/rhessi3/mission/science/the-impact-of-flares/index.html. (Accessed 27 January 2020).

Hoeksema, J.T., Liu, Y., Hayashi, K., Sun, X., Schou, J., Couvidat, S., Norton, A., Bobra, M., Centeno, R., Leka, K., et al., 2014. The helioseismic and magnetic imager (HMI) vector magnetic field pipeline: overview and performance. Sol. Phys. 289, 3483–3530.

Joint Science Operations Center, 2019a. HARP - HMI Active Region Patches. http://jsoc.stanford.edu/jsocwiki/HARPDataSeries. (Accessed 18 December 2019).

Joint Science Operations Center, 2019b. Science Data Processing. http://jsoc.stanford.edu/. (Accessed 23 July 2019).

Joint Science Operations Center, 2019c. SpaceWeather HMI Active Region Patch (SHARP). http://jsoc.stanford.edu/doc/data/hmi/sharp/sharp.htm. (Accessed 8 August 2019).

Joint Science Operations Center, 2020. Line-of-Sight magnetograms. http://jsoc.stanford.edu/HMI/Magnetograms.html. (Accessed 10 February 2020).

Kazachenko, M.D., Lynch, B.J., Welsch, B.T., Sun, X., 2017. A database of flare ribbon properties from the solar Dynamics observatory. I. Reconnection flux. Astrophys. J. 845, 49.

Liu, J., Lin, C.H., Tsai, H., Liou, Y., 2004. Ionospheric solar flare effects monitored by the ground-based GPS receivers: theory and observation. J. Geophys. Res.: Space Physics 109.

Loper, R., 2018. Reconnection signatures in solar magnetograms. In: Proceedings of the 2018 AGU Fall Meeting. SH14B-04. AGU, Washington, D.C., 2018.

Mason, J., Hoeksema, J., 2010. Testing automated solar flare forecasting with 13 Years of Michelson Doppler imager magnetograms. Astrophys. J. 723, 634.

Qian, L., Burns, A.G., Solomon, S.C., Chamberlin, P.C., 2012. Solar flare impacts on ionospheric electrodyamics. Geophys. Res. Lett. 39.

Scherrer, P.H., Schou, J., Bush, R., Kosovichev, A., Bogart, R., Hoeksema, J., Liu, Y., Duvall, T., Zhao, J., Schrijver, C., et al., 2012. The helioseismic and magnetic imager (HMI) investigation for the solar Dynamics observatory (SDO). Sol. Phys. 275, 207–227.

Schou, J., Scherrer, P.H., Bush, R.I., Wachter, R., Couvidat, S., Rabello-Soares, M.C., Bogart, R.S., Hoeksema, J.T., Liu, Y., Duvall, T.L., Akin, D.J., Allard, B.A., Miles, J. W., Rairden, R., Shine, R.A., Tarbell, T.D., Title, A.M., Wolfson, C.J., Elmore, D.F., Norton, A.A., Tomczyk, S., 2012. Design and ground calibration of the helioseismic and magnetic imager (HMI) instrument on the solar Dynamics observatory (SDO). Sol. Phys. 275, 229–259. https://doi.org/10.1007/s11207-011-9842-2.

Space Weather Prediction Center, 2009. Implement XRS Event Detection. http://intranet/wiki/index.php?title=GOES-NOP:PPNCR0078&oldid=11361. (Accessed 19 December 2019).

Space Weather Prediction Center, 2019. Data archive. retrieved on 25 September 2019. ftp://ftp.swpc.noaa.gov/pub/warehouse/.

Stanford University, 2019. Helioseismic and Magnetic Imager. http://hmi.stanford.edu/Description/hmi-overview/hmi-overview.html. (Accessed 19 November 2019).

Verma, M., 2018. The origin of two X-class flares in active region NOAA 12673-shear flows and head-on collision of new and preexisting flux. Astron. Astrophys. 612, A101.

Wheatland, M., 2008. The energetics of a flaring solar active region and observed flare statistics. Astrophys. J. 679, 1621.